THE ASTROPHYSICAL JOURNAL, 424:222–236, 1994 March 20

STRUCTURE AND CHEMISTRY IN THE NORTHWESTERN CONDENSATION OF THE SERPENS MOLECULAR CLOUD CORE

JOSEPH P. MCMULLIN AND LEE G. MUNDY
Astronomy Department, University of Maryland, College Park, MD 20742
BRUCE A. WILKING AND T. HEZEL
Physics Department, University of Missouri – St. Louis, 8001 Natural Bridge Road, St. Louis, MO 63121
AND
GEOFF A. BLAKE
Division of Geological and Planetary Sciences, California Institute of Technology, 170-25, Pasadena, CA 91125
Received 1993 May 28; accepted 1993 September 23

ABSTRACT

We present single-dish and interferometric observations of gas and dust in the core of the Serpens molecular cloud, focusing on the northwestern condensation. Single-dish molecular line observations are used to probe the structure and chemistry of the condensation while high-resolution images of CS and CH_3OH are combined with continuum observations from $\lambda = 1.3$ mm to $\lambda = 3.5$ cm to study the subcondensations and overall distribution of dust.

For the northwestern condensation, we derive a characteristic density of 3×10^5 cm^{-3} and an estimated total mass of $\sim 70\ M_\odot$. We find compact molecular emission associated with the far-infrared source S68 FIRS 1, and with a newly detected subcondensation named S68 N. Comparison of the large- and small-scale emission reveals that most of the material in the northwest condensation is *not* directly associated with these compact sources, suggesting a youthful age for this region. CO $J = 1 \rightarrow 0$ observations indicate widespread outflow activity. However, no unique association of embedded objects with outflows is possible with our observations. The SiO emission is found to be extended with the overall emission centered about S68 FIRS 1; the offset of the peak emission from all of the known continuum sources and the coincidence between the blueshifted SiO emission and blueshifted high-velocity gas traced by CO and CS is consistent with formation of SiO in shocks. Derived abundances of CO and HCO^+ are consistent with quiescent and other star-forming regions while CS, HCN, and H_2CO abundances indicate mild depletions within the condensation.

Spectral energy distribution fits to S68 FIRS 1 indicate a modest luminosity (50–60 $L_\odot$), implying that it is a low-mass (0.5–3 $M_\odot$) young stellar object. Radio continuum observations of the triple source toward S68 FIRS 1 indicate that the lobe emission is varying on timescales $\leqslant 1$ yr while the central component is relatively constant over ~ 14 yr. The nature of a newly detected compact emission region, S68 N, is less certain due to the absence of firm continuum detections; based on its low luminosity ($< 5\ L_\odot$) and strong molecular emission, S68 N may be a prestellar subcondensation of gas and dust.

Subject headings: ISM: clouds — ISM: individual (Serpens) — ISM: molecules — molecular processes

1. INTRODUCTION

Millimeter and submillimeter wavelength observations are providing a growing list of young stellar objects (YSOs) which are deeply embedded in circumstellar gas and dust (e.g., Wilking, Lada, & Young 1989; Andre et al. 1990; Walker, Adams, & Lada 1990). These objects, which span a vast range in both bolometric luminosity (~ 1–$10^5\ L_\odot$) and mass of the surrounding material (0.01–100's of $M_\odot$), are likely to be the youngest stellar members of our Galaxy. As such, they provide the best laboratory for examining early pre–main-sequence evolution. Those studies, which have concentrated on individual members of this class, have detected emission from a wide variety of molecular species. Through comparisons of emission distributions, these observations have helped to characterize the properties and associated timescales of these poorly understood stages of a star's life (e.g., McMullin, Mundy, & Blake 1993; Goldsmith et al. 1992; Blake et al. 1987; Plambeck & Wright 1987). Systematic studies of the diverse molecular morphology in the earliest stellar stages are essential to identifying the underlying physical and chemical processes which shape the appearance and chemistry of material associated with and participating in the formation of a YSO.

The Serpens molecular cloud presents an excellent opportunity for studying the physics and chemistry of star formation due to its proximity ($d \sim 310$ pc; de Lara, Chavarria-K, & Lopez-Molina 1991) and abundance of young objects (e.g., Strom, Grasdalen, & Strom 1974; Gomez de Castro, Eiroa, & Lenzen 1988; Eiroa & Casali 1992). The Serpens molecular cloud was first recognized as a potential site of star formation through the identification of embedded IR objects and associated reflection nebulae (Strom et al. 1974; Strom, Vrba, & Strom 1976). Subsequent studies of the region in NH_3, H_2CO, and far-infrared continuum emission have defined a core region composed of two dense condensations separated by $\sim 3'$ (Ho and Barrett 1980; Little et al. 1980; Ungerechts & Güsten 1984; Harvey, Wilking, & Joy 1984; Zhang, Laureijs, & Clark, 1988a). Estimates of the total luminosity of the Serpens core (200 $L_\odot$, Nordh et al. 1982; 85 $L_\odot$, Zhang et al. 1988b, both scaled to a distance of 310 pc) combined with the large number of embedded IR sources (> 50;

Eiroa & Casali 1992) suggest that mainly low-mass stars are forming in the region. The southeastern condensation is dominated by SVS-20, a pre–main-sequence infrared double source (Eiroa et al. 1987). Near-infrared images of the region show that the majority of early stellar objects (mostly reddened T Tauri-like stars) are located in the region surrounding SVS-20 (Eiroa & Casali 1992; Churchwell & Koorneef 1986). The lower number of T Tauri-like stars in the northwest condensation suggests that it is in an earlier evolutionary state (Nordh et al. 1982; Eiroa & Casali 1992). In particular, the northwestern condensation is associated with some of the "classic" signatures of early star formation: high-velocity gas motions as indicated by CO and OH observations (Loren, Evans, & Knapp 1979; Bally and Lada 1983; Snell & Bally 1986; Mirabel et al. (1987) along with H_2O masers (e.g., Rodriguez et al. 1980).

S68 FIRS 1 (IRAS 18273+0113) is the strongest far-infrared source in the Serpens core and appears to be an excellent candidate for a deeply embedded YSO. It is located in the northwestern condensation at peaks in the NH_3 and H_2CO emission (Ungerechts & Güsten 1984; Ho & Barrett 1980; Loren et al. 1979) and has substantial energetic activity associated with it (H_2O masers, Dinger & Dickinson 1980; Rodriguez et al. 1980; jetlike H_2 emission, Eiroa & Casali 1989). Recent attention has focused on this object due to its peculiar radio emission (Rodriguez et al. 1980; Rodriguez et al. 1989). Simultaneous observations at $\lambda = 2$ cm and $\lambda = 6$ cm have revealed that the emission consists of a central component with a spectral index of 0.1, and two lobes with spectral indices ≤ -0.6, values characteristic of nonthermal emission. Comparison of observations from 1978, 1984, and 1989 (Rodriguez et al. 1989) indicates that the outer lobes are in fact moving away from the central source at a rate of $0''.12$ yr^{-1}, corresponding to a projected velocity of ~ 200 km s^{-1} at a distance of 310 pc.

In this paper, we present single-dish and interferometric observations which focus on the northwestern condensation in the Serpens molecular core and in particular on the source S68 FIRS 1. The identification of the central radio source toward S68 FIRS 1 as the embedded YSO is confirmed through comparison of millimeter and centimeter interferometric observations. We also report on a second compact emission region, approximately 2′ north of S68 FIRS 1. The second region, hereafter labeled S68 N, is a source of strong molecular emission and may be associated with extended far-infrared emission, north of S68 FIRS 1.

2. OBSERVATIONS

Observations were obtained toward S68 FIRS 1 and S68 N using the following reference positions: S68 FIRS 1, $\alpha(1950) = 18^h27^m17^s.5$, $\delta(1950) = 1°13'06''.5$; and S68 N, $\alpha(1950) = 18^h27^m15^s.9$, $\delta(1950) = 1°14'49''$, as defined by preliminary $\lambda = 1.25$ mm continuum data.

2.1. *Single Dish*

Single dish observations at $\lambda = 2.6$ and 1.3 mm were obtained with the NRAO[1] 12 m telescope during runs from 1991 May through 1992 June using the facility dual polarization receivers. Table 1 outlines the molecules, transitions, velocity resolutions, beam sizes, and typical rms noise levels. The system temperature of each polarization channel was ~ 350 K single-sideband. The spectrometer was configured as two dual polarization 128 channel filterbanks with 100 kHz resolution and a 128 channel filterbank with 30 kHz resolution (except for CO, which employed two filterbanks with 250 and 100 kHz resolution). Calibration was accomplished using the chopper wheel method, and the resulting data are reported as T_R^* value (Kutner & Ulich 1981) or as T_{MB}, using a "corrected" main beam efficiency of $\eta_m^* = 0.83$ (Jewell 1988) at 98 GHz and 0.48 at 230 GHz. Maps were acquired using absolute position switching to a reference position 20′ W and 20′ S of S68 FIRS 1. The CS $J = 2 \rightarrow 1$, CO $J = 1 \rightarrow 0$, and SiO $J = 2 \rightarrow 1$ maps cover the peak emission in the area. The C ^{34}S $J = 2 \rightarrow 1$ and C ^{18}O $J = 2 \rightarrow 1$ data consist of 30″ and 15″ spacing crosses,

[1] The National Radio Astronomy Observatory is operated by Associated Universities, Inc., under cooperative agreement with the National Science Foundation.

TABLE 1

MOLECULAR LINE OBSERVATIONS

Transition	Observatory	Rest Frequency (GHz)	Velocity Resolution (km s^{-1})	Beam Size (″)	Typical rem Noise (K)
HDO $1_{1,0}$–$1_{1,1}$	NRAO 12 m	80.578	0.37	74	0.04
H ^{13}CO$^+$ $J = 1 \rightarrow 0$	NRAO 12 m	86.754	0.35	68	0.06
SiO $J = 2 \rightarrow 1$	NRAO 12 m	86.847	0.35	68	0.05
C ^{34}S $J = 2 \rightarrow 1$	NRAO 12 m	96.413	0.31	62	0.05
CS $J = 2 \rightarrow 1$	NRAO 12 m	97.981	0.31	61	0.13
CO $J = 1 \rightarrow 0$	NRAO 12 m	115.272	0.65	52	0.23
C ^{18}O $J = 2 \rightarrow 1$	NRAO 12 m	219.560	0.34	27	0.27
C ^{34}S $J = 5 \rightarrow 4$	CSO	241.016	0.59	31	0.05
CS $J = 5 \rightarrow 4$	CSO	244.936	0.59	30	0.12
CH_3OH $7_0 \rightarrow 6_0$ A$^+$	CSO	338.409	0.43	20	0.07
CS $J = 7 \rightarrow 6$	CSO	342.883	0.43	20	0.22
CO $J = 3 \rightarrow 2$	CSO	345.796	0.43	20	0.1
H_2CO $5_{15} \rightarrow 4_{14}$	CSO	351.769	0.41	20	0.15
HCN $J = 4 \rightarrow 3$	CSO	352.506	0.41	20	0.15
HCO$^+$ $J = 4 \rightarrow 3$	CSO	356.734	0.41	20	0.15
CS $J = 2 \rightarrow 1$	BIMA	97.981	0.31	15 × 10[a]	0.5[b]
CH_3OH $8_0 \rightarrow 7_1$ A$^+$	BIMA	95.169	0.31	15 × 10[a]	0.5[b]

[a] Position angle of the beam is $-14°$; beam size for S68 N is 12″ × 6″ with a positional angle of $-5°$.
[b] Jy beam^{-1}.

respectively. Five point crosses with 30″ spacings were obtained in $H^{13}CO^+$ $J = 1 \rightarrow 0$ toward S68 FIRS 1 and S68 N. Individual spectra toward S68 FIRS 1 and S68 N were acquired in HDO $1_{1,0}$–$1_{1,1}$. Negative fluxes in the blue wing of the CO $J = 1 \rightarrow 0$ emission at the edge of the core indicate that some CO $J = 1 \rightarrow 0$ emission was present in the reference position; the CO $J = 1 \rightarrow 0$ blue wing results therefore represent lower limits to the true emission.

At shorter wavelengths, a partial molecular line survey of the region was performed at the Caltech Submillimeter Observatory (CSO).[2] Spectral line observations toward S68 FIRS 1 and S68 N, using the facility 230 and 345 GHz receivers, were carried out in observing runs from 1989 August to 1992 June. Weather conditions were characterized by $\tau(225\ \mathrm{GHz}) \sim 0.15$; typical single-sideband system temperatures ranged from 600 to 700 K. The facility 1024 channel acousto-optical spectrometers with 50 and 500 MHz total bandwidth were utilized; the corresponding velocity resolutions, along with the typical rms noise for each observation are given in Table 1. The antenna temperatures, T_A^*, were converted to main beam temperatures using $\eta_m = 0.74$ at 230 GHz and 0.62 at 345 GHz.

A map of dust emission in the $\lambda = 1.25$ mm continuum was also made at the CSO using a beam size of 30″. Observations were obtained at half-beam intervals using the facility bolometer system with a 2′ chopper throw in azimuth. Primary calibration was established with respect to Uranus (93 K) and Mars (209 K); IRAS 16293−2422 (6.7 Jy) and 3C 273 (25.1 Jy) were used as secondary calibrators. Corrections to the continuum flux densities were calculated based on integration of an atmospheric transmission model over the filter bandpass (Keene 1991). Regular measurements of the atmospheric opacity at 225 GHz toward the zenith were made to follow variations in the opacity with time. Our reported fluxes are effective fluxes at the mean filter frequency (239.6 GHz) assuming a ν^3 spectral dependence for the intrinsic source emission. Uncertainty in the overall flux calibration is estimated to be 15%. Effective "color corrections" for ν^2 and ν^4 spectral dependences are 1.07 and 0.91, respectively. The resulting rms noise in the map was approximately 0.06 Jy beam^{-1}. Pointing was established through observations of Uranus; errors were typically less than 5″. The position angle of the chopper varied from 44° to 66° during the observations.

2.2. *Interferometer*

Spectral line and continuum data toward S68 FIRS 1 and S68 N were obtained using the three-element BIMA[3] array between 1990 September and 1992 May. The 512 channel digital correlator was arranged to observe CS $J = 2 \rightarrow 1$ and CH_3OH $J_K = 8_0$–7_1 A^+ in the upper and lower sideband, respectively, of a 10 MHz band. Continuum observations were simultaneously taken in two 40 MHz bands with the digital correlator and in 150 MHz band with the analog correlator. Eight configurations of the three-element array were employed with projected antenna spacings ranging from 2 kλ to 30 kλ. Naturally weighted synthesized beams of 12″ × 6″ and 11″ × 6″ were obtained for the CS and continuum observations of S68 N and 15″ × 10″ and 15″ × 11″ for the CS and continuum observations of S68 FIRS 1. At 97.981 GHz, the 6.1 m diameter antennas have a primary beam width of 2.′0. The compact sources NRAO 530, 2145 + 067, and 1749 + 096 were used as phase calibrators. The flux scale was established from observations of Saturn and Venus (Ulich 1981; Ulich, Dickel, & de Pater 1984). NRAO 530, 2145+067, and 1749+096 were adopted as secondary calibration standards using flux densities of 5.5, 4.1, and 2.5 Jy, respectively, for the 1990 observations and 5.1 and 3.7 Jy for the 1992 observations (1749+096 was not used in 1992). The single-sideband system temperature during the observations was generally ∼600 K.

A line-free continuum map was formed by averaging the channels in a correlator band showing no line emission. Spectral line maps were made by subtracting the dirty continuum maps from the dirty spectral line maps. The data were then CLEANed using the MIRIAD[4] package. Typical rms noise values for the CLEANed maps are 0.4 Jy beam^{-1} for the CS and CH_3OH data, and 0.014 Jy beam^{-1} for the $\lambda = 3.1$ mm continuum. No correction for primary beam taper has been applied.

Continuum observations of S68 FIRS 1 and S68 N at $\lambda = 2.0$ and $\lambda = 1.3$ cm were made on 1992 April 20 using the NRAO VLA in the C-configuration. The absolute flux density calibrator was 3C 286, with adopted flux densities of 3.5 and 2.5 Jy at $\lambda = 2.0$ and $\lambda = 1.3$ cm, respectively. The phase calibrator was 1741−038, with bootstrapped fluxes of 3.7 and 4.4 Jy. Additional observations were obtained in 1993 February at $\lambda = 2.0$, 3.6, and 6.0 cm in the D-configuration. The absolute flux density calibrator and phase calibrator were the same as the first observations, with adopted fluxes for 3C 286 of 3.5 Jy, 5.3 Jy, and 7.6 Jy at $\lambda = 2.0$, 3.6, and 6.0 centimeters, and bootstrapped fluxes for 1741−038 of 4.2 Jy, 3.3 Jy, and 2.6 Jy. The data were edited and calibrated following the standard VLA procedures in AIPS.

3. RESULTS

3.1. *Large-Scale Structure*

Figure 1 shows the distribution of peak temperature in the CS $J = 2 \rightarrow 1$ transition in the Serpens core. The emission peaks strongly around SVS-20 (∼4 K) with a weaker plateau of emission (∼2 K) extending to the northwest, toward S68 FIRS 1 and S68 N. Typical line widths are 3 km s^{-1}. Compared to previous molecular and far-infrared studies, the overall extent of the core appears to be well-traced by the CS emission. However, the dominance of the southeastern condensation contrasts sharply with NH_3 and H_2CO emission in the region which show the southeastern and northwestern condensations to have peaks of nearly equal strength (Ungerechts & Güsten 1984). Dust continuum emission at $\lambda = 50$ and 100 μm is strongest in the northwestern condensation (Zhang et al. 1988a). No specific CS peak is apparent around the position of S68 FIRS 1 (IRAS 18273+0113).

Figure 2 shows CS and $C^{34}S$ spectra toward S68 FIRS 1 and S68 N. Both sources show modest self-absorptions in CS $J = 2 \rightarrow 1$ at the cloud velocity (∼8.5 km s^{-1}) as indicated by $C^{34}S$ spectra which peak at the velocity of the dip in the CS $J = 2 \rightarrow 1$ spectra. The CS $J = 5 \rightarrow 4$ and $J = 7 \rightarrow 6$ spectra do not show self-absorptions. For S68 N, the line width in the $J = 5 \rightarrow 4$ transition is similar to the $J = 2 \rightarrow 1$ transition; for S68 FIRS 1, there appear to be two components, a core with a

[2] The Caltech Submillimeter Observatory is operated by the California Institute of Technology under funding from the US National Science Foundation (no. AST 90-15755).

[3] Berkeley, Illinois, and Maryland Association.

[4] Multichannel Image Reconstruction, Image Analysis, and Display software developed by the Berkeley, Illinois, and Maryland Association.

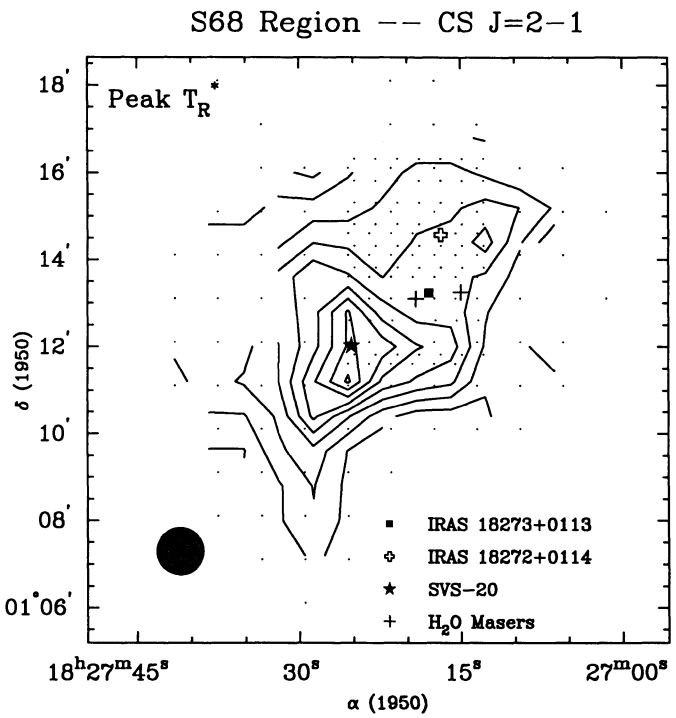

FIG. 1.—Map of the peak temperature in the CS $J = 2$–1 transition acquired with the NRAO 12 m telescope. Contour levels are in steps of 0.5 K starting at 0.5 K. Dots mark scan positions for the observations. The box and hollow cross mark the location of IRAS 18273+0113 and IRAS 18272+0014; the solid crosses mark the locations of assoiated H_2O masers. SVS-20 is represented by the star symbol. IRAS 18273+0113 is identified with S68 FIRS 1.

width of ~ 3 km s^{-1} superposed on a broad (~ 10 km s^{-1}), weak plateau. The CS $= 7 \rightarrow 6$ spectra exhibits similar structure, displaying broad, predominantly red wing emission; Fuller & Ladd (1992) have also identified two velocity components in their CS $J = 7 \rightarrow 6$ observations.

A map of the $\lambda = 1.25$ mm dust emission toward S68 FIRS 1 is presented in Figure 3. These data show a strong central peak (2.3 Jy beam^{-1}) near S68 FIRS 1, with some extended emission. Integrating the flux over the map yields a total flux of 6.5 Jy. Pointed observations toward S68 N at $\lambda = 1.25$ mm indicate a flux of ~ 0.9 Jy beam^{-1} or greater; the lower limit is caused by contamination of the OFF position by S68 FIRS 1; it was not possible to map S68 N due to contamination. Comparing Figures 1 and 3, the 30″ resolution continuum emission is obviously more strongly peaked on S68 FIRS 1 than the 60″ resolution CS $J = 2 \rightarrow 1$ emission.

3.2. *Small-Scale Structure*

The millimeter wavelength interferometric observations reveal compact emission associated with both S68 FIRS 1 and S68 N. The left panel in Figure 4 shows the CS $J = 2 \rightarrow 1$ integrated intensity map composed of all channels with 4 σ or greater emission. For S68 FIRS 1, the emission region is approximately 30″ in size and shows no discernible velocity pattern (Fig. 5). The peak integrated emission is weak compared with S68 N (8.4 vs. 19.5 Jy beam^{-1} km s^{-1} for S68 N). The CS emission around S68 N shows an overall ridgelike structure which breaks into multiple components in some velocity intervals (Fig. 6); a velocity gradient is apparent with redder emission positioned to the southeast and bluer emission positioned to the northwest. Comparison with the single-dish observations indicates that 40% to 50% of the CS emission is recovered in the interferometer maps of S68 N, while on $\sim 14\%$ of the CS emission from the S68 FIRS 1 region is recovered.

A map of the velocity-integrated methanol emission is shown in the right panel of Figure 4. Compact methanol emission was detected toward S68 N; no emission was detected from the S68 FIRS 1 region.

Interferometer observations of the $\lambda = 3.1$ mm continuum are shown in the center panel of Figure 4. S68 FIRS 1 was detected with a peak flux of 140 mJy beam^{-1} The emission, which is unresolved in our beam (15″ × 11″), is located within the *IRAS* error ellipse (shown as dashed lines in Fig. 4, center panel), and coincides with the weak CS peak. No continuum emission was detected toward S68 N to a level of 36 mJy beam^{-1} (3 σ).

Observations of the centimeter wavelength continuum toward S68 FIRS 1 detected the triple radio source seen by Rodriguez et al. (1989). Figure 7 shows an overlay of the $\lambda = 2.0$ cm continuum emission (white contours) on the $\lambda = 3.1$ mm continuum map (grayscale and black contours). The $\lambda = 3.1$ mm source is clearly associated with the central component, supporting the contention (Torrelles et al. 1992) that it is the exciting source. No centimeter wavelength emission was detected from the S68 N region; we derive upper limits (3 σ) of 0.4 mJy beam^{-1} and 0.85 mJy beam^{-1} for $\lambda = 2.0$ and $\lambda = 1.3$ cm, respectively. Table 2 summarizes the continuum observations for the two sources.

Figure 8 shows a plot of the radio continuum flux versus wavelength for each component of the triple source, along with the $\lambda = 3.1$ mm continuum flux. The centimeter wavelength spectral indices for the lobes, derived from observations in 1993 April, are inconsistent with the previous study by Rodriguez et al. (1989). We measured fluxes for the southeastern lobe of 2.2 mJy beam^{-1} and 3.9 mJy beam^{-1} at $\lambda = 2.0$ and $\lambda = 1.3$ cm, respectively; the northwestern lobe had fluxes of 0.9 mJy beam^{-1} and 1.1 mJy beam^{-1} at $\lambda = 2.0$ and $\lambda = 1.3$ cm. We saw no evidence for the steeply negative spectral slopes in the lobes; instead, the derived spectral indices were positive and consistent with thermal emission. The relative brightness of the southeast and northwest lobes was also different, with the southeast lobe brighter in our observations. The fact that our $\lambda = 2.0$ cm flux and spectral index for the central component

TABLE 2

CONTINUUM OBSERVATIONS

Wavelength	S68 FIRS 1	S68 N
12 μm	0.25L Jy[a]	
20 μm	2.6 Jy[b]	
25 μm	3.17L Jy[a]	
50 μm	88.6 Jy[b]	<16 Jy[c]
60 μm	152.92 Jy[a]	
100 μm	380 Jy[b]	<20 Jy[c]
160 μm	430 Jy[b]	
1.25 mm	2.3 Jy	≤0.9 Jy
3.1 mm	140 mJy	<36 mJy
1.3 cm	5.3 mJy[d]	<0.9 mJy
2.0 cm	4.8 mJy[d]	<0.4 mJy
3.5 cm	2.8 mJy[d]	
6.0 cm	2.2 mJy[d]	

[a] From the *IRAS* Point Source Catalog.
[b] From Harvey, Wilking, & Joy 1984.
[c] From Zhang et al. 1988, Fig. 1*a* and 1*b*.
[d] Central source only.

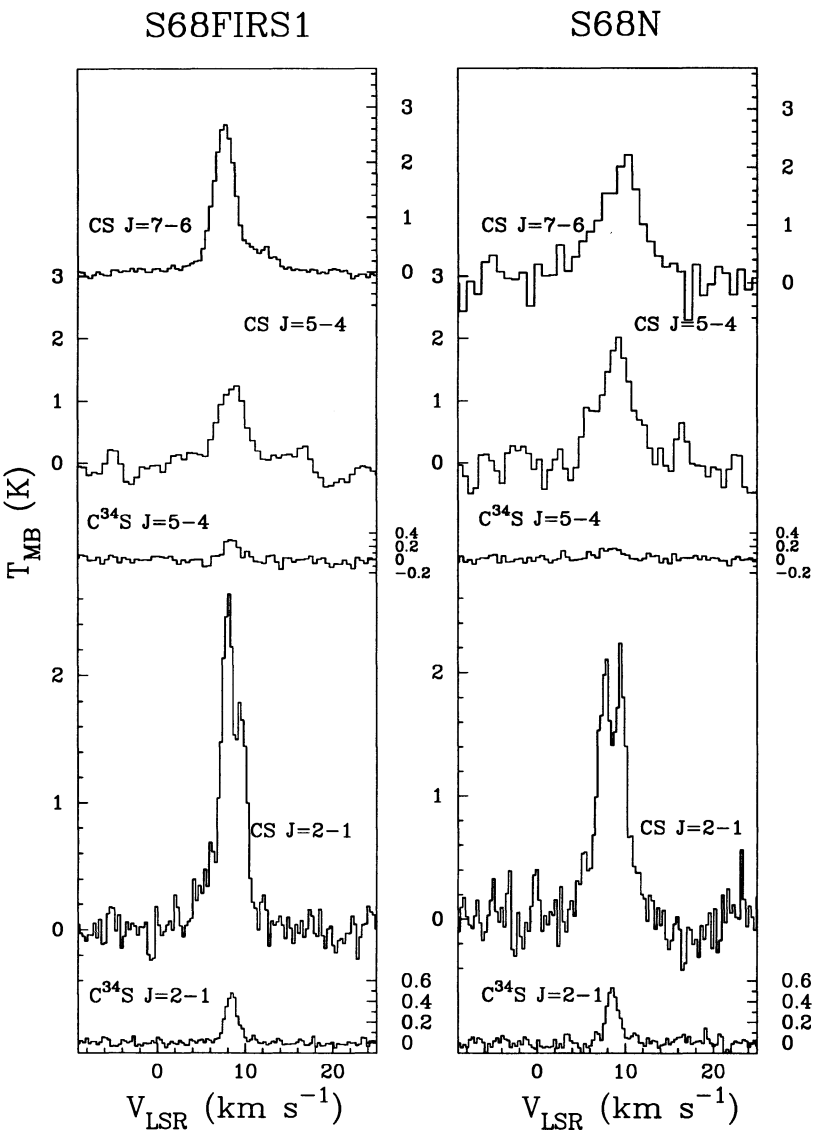

FIG. 2.—Spectra of the C ^{34}S $J = 5$–4, CS $J = 5$–4, and CS $J = 7$–6 (CSO) and C ^{34}S $J = 2$–1 and CS $J = 2$–1 (NRAO 12 m) used in deriving the physical conditions within the northwestern condensation. The vertical axis is main beam brightness temperature; the scale for each spectrum is displayed along the edge.

were consistent with Rodriguez et al. (1989) suggested that the lobe emission had varied. This variability is confirmed by the more recent observations which demonstrate a drastic change in the emission of the lobes in less than a year (Fig. 8); the $\lambda = 2.0$ cm emission in the southeastern lobe has changed from 2.2 mJy beam^{-1} to 0.6 mJy beam^{-1} while the northwestern lobe had changed from 1.1 mJy beam^{-1} to 0.7 mJy beam^{-1}. The spectral slopes have also changed from positive to negative. The southeastern lobe is significantly brighter at longer wavelengths, having a flux density of 3.0 and 2.1 mJy beam^{-1} at $\lambda = 6.0$ and 3.5 cm; the northwestern lobe has a flux density of 1.3 and 1.4 mJy beam^{-1} at $\lambda = 6.0$ and 3.5 cm. The central component is once again consistent with previous observations. Recent observations by Curiel et al. (1993) have also noted a change in the spectral indices of the lobes. Comparison of data from Rodriguez et al. (1980) and Rodriguez et al. (1989) suggests that the southeastern lobe changed by a factor of 2 in flux between those epochs. Mechanisms have been proposed which can account for both the nonthermal indices seen by Rodriguez et al. (1989) (diffusive shock acceleration, Crusius-Watzel 1990) and for the variation between thermal and nonthermal indices (Henriksen, Ptuskin, & Mirabel 1991). More detailed observations are needed to monitor this variability and see if the properties of the lobes are temporally correlated.

3.3. *Tracing the Energetic Activity:* CO, CS, *and* SiO

Figure 9*a* shows the distribution of CO $J = 1 \rightarrow 0$ emission. The emission again peaks on SVS-20, with an extension toward S68 FIRS 1 and S68 N but no obvious secondary peaking on either source. Below this, in Figure 9*b*, the integrated CO emission from the blue line wings (-4 to 5 km s^{-1}) in gray contours and the redline wings (11–20 km s^{-1}) in black contours display regions of strong outflow activity. These contours indicate only the strongest activity; other areas have lower levels of high-velocity emission which are lost in the overall confusion of the region; spectra taken toward S68 FIRS 1 and S69 N both show extended wings. No unique association of outflow emission with specific objects was pos-

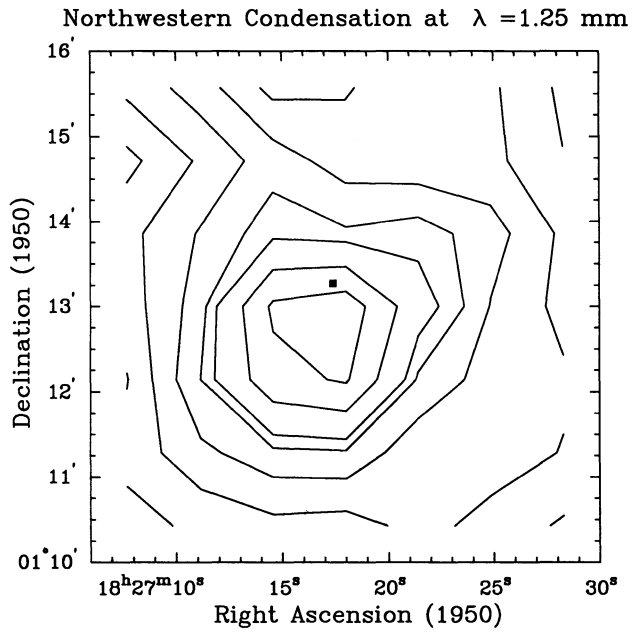

FIG. 3.—$\lambda = 1.25$ mm continuum emission from S68 FIRS 1. Contours are levels of 0.2, 0.4, 0.6, 0.8, 1.0, 1.5, and 2.0 Jy beam^{-1}. The solid box marks the position of S68 FIRS 1. The peak value is 2.3 Jy beam^{-1}.

sible with the CO $J = 1 \rightarrow 0$ data. Comparing our CO data to previous observations reveals a more complex structure than the lower resolution maps of Bally & Lada (1983) and confirms the morphology reported by Allen et al. (1989). Figure 9*c* displays the integrated CS $J = 2 \rightarrow 1$ emission. The contours trace the molecular core also seen in NH_3 and H_2CO. Separating blueshifted and redshifted emission from the integrated CS $J = 2 \rightarrow 1$ maps, we also see indications of outflow activity. The gray (black) contours in Figure 9*d* show the blue (red) emission. As is the case for CO, it is unclear how the emission is tied to the embedded infrared objects.

Figure 10 shows the SiO $J = 2 \rightarrow 1$ emission from the Serpens core integrated in velocity from 0 to 11 km s^{-1} (grayscale and black contours). The emission is distributed in an elongated structure aligned southeast–northwest, about S68 FIRS 1. S68 N falls at the rough location of the peak in the northwestern lobe; SVS-20 is located at the edge of the southeastern lobe and does not appear to be associated with SiO emission.

The SiO spectra show a characteristic FWZI (full width at zero intensity) of ~ 6 km s^{-1}, with a distinctive blue wing in a localized region southeast of S68 FIRS 1. Integrating only the emission from 0 to 5 km s^{-1}, we get the overlaid white contours on Figure 10. The location of the blue wing emission is coincident with blueshifted emission in CS $J = 2 \rightarrow 1$ and CO

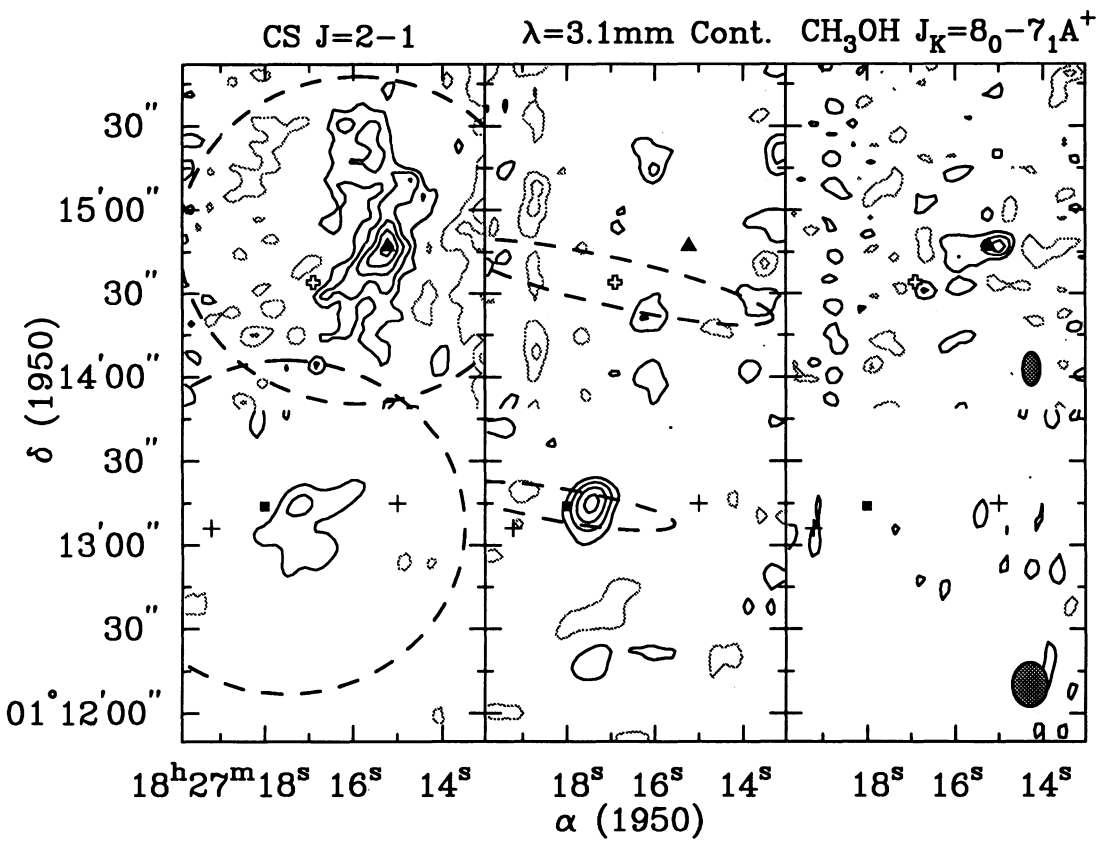

FIG. 4.—Mosaiced integrated intensity maps of S68 FIRS 1 and S68 N. The dashed circles to the left panel denote the size of the primary beam for the two interferometer observations. The dashed curves in the center panel represent the error ellipses for the associated *IRAS* sources. The synthesized beams for each pointing center are shown in the right panel. The contour levels for the molecular emission are in steps of 3.6 Jy beam^{-1} km s^{-1} for CS and 3.0 Jy beam^{-1} km s^{-1} for CH_3OH. For S68 FIRS 1, the molecular emission was integrated from 7 to 12 km s^{-1}; for S68 N, the emission was integrated from 2 to 16 km s^{-1} for CS and from 3 to 11 km s^{-1} for the CH_3OH emission. For the $\lambda = 3$ mm continuum emission, the contours are in steps of 0.03 Jy beam^{-1}. The box marks the position of the *IRAS* source associated with S68 FIRS 1; the triangle marks the position of S68 N as determined from the CS emission in the left panel. The solid crosses mark the H_2O maser positions and the hollow cross marks the position of IRAS 18272 + 0114.

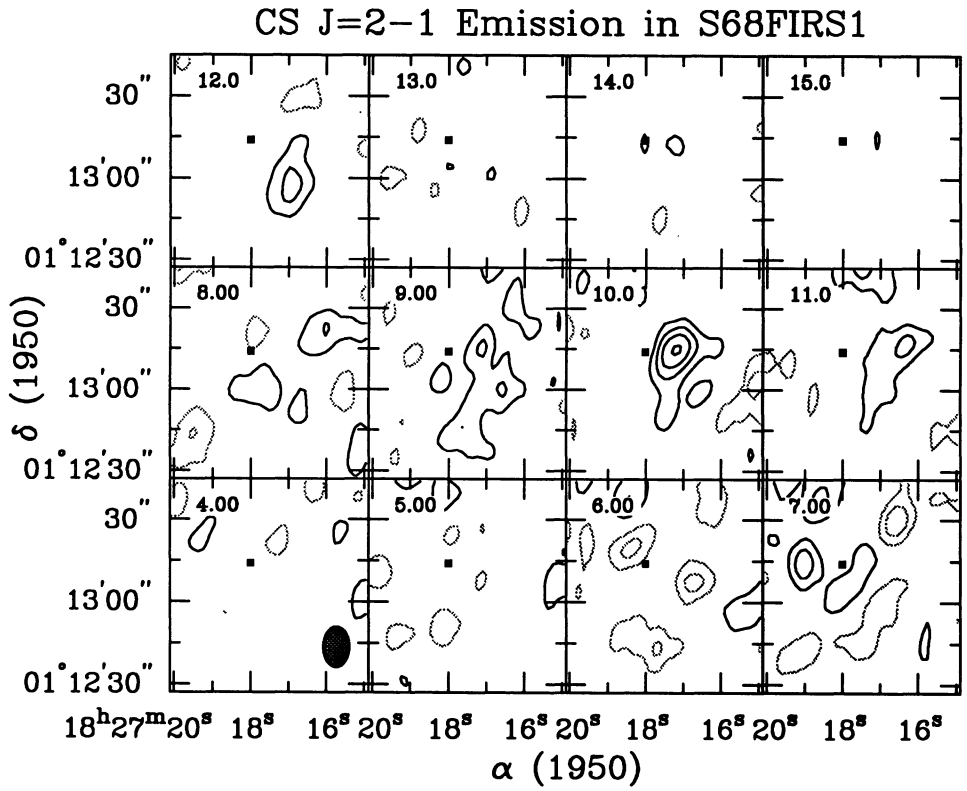

FIG. 5.—Channel maps of the CS $J = 2$–1 emission toward S68 FIRS 1 in 1 km s^{-1} bins. Contour levels are in steps of 2 $\sigma = 0.42$ Jy beam^{-1}. The beam is shown in the lower left box. The square marks the position of IRAS 18273 + 0113. The numbers in the upper left of each box are the velocity in km s^{-1}.

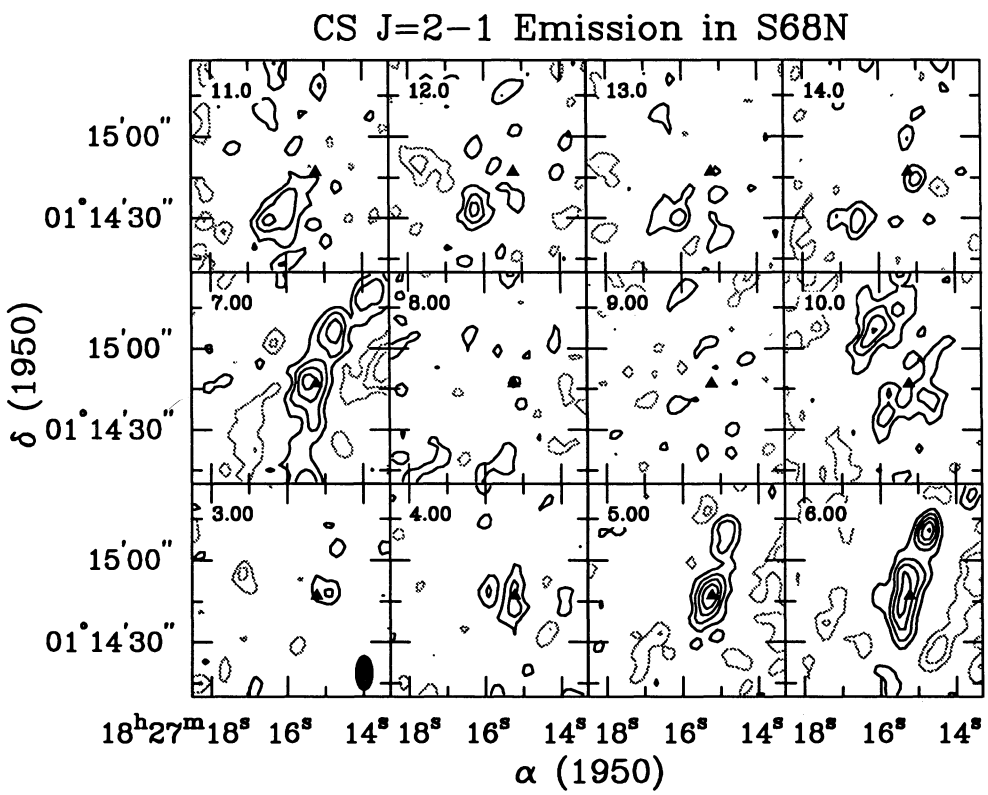

FIG. 6.—Channel maps of the CS $J = 2$–1 emission toward S68 N in 1 km s^{-1} bins. Contour levels are in steps of 2 $\sigma = 0.42$ Jy beam^{-1}. The beam is shown in the lower left box. The solid triangle marks the position of S68 N, as determined from the peak integrated CS $J = 2$–1 intensity.

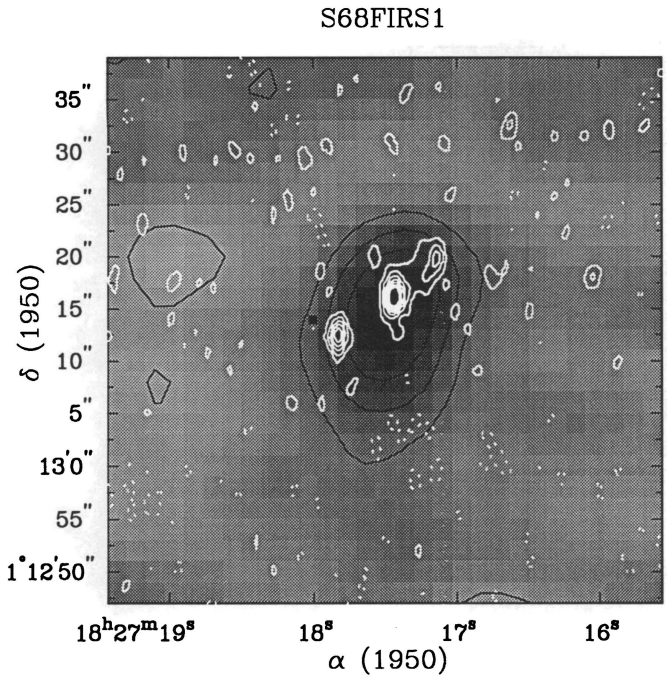

FIG. 7.—Continuum emission from S68 FIRS 1. The grayscale and black contours represent the $\lambda = 3.1$ mm emission. Contours are in steps of $2\ \sigma = 0.32$ mJy beam^{-1}. The $\lambda = 3.1$ mm emission is coincident with the central $\lambda = 2.0$ cm source to within the positional uncertainty.

$J = 1 \rightarrow 0$ shown in Figure 10. The dearth of SiO emission at SVS-20 suggests that the wing is associated with S68 FIRS 1.

3.4. *Chemical Survey*

We have initiated a molecular line survey toward S68 FIRS 1 and S68 N. Figures 11 and 12 display the results to date, indicating a rich chemistry for both regions Observations of SiO $J = 7 \rightarrow 6$ and HDO $1_{10} \rightarrow 1_{11}$ were also obtained with no detections at the 3 σ level (see Table 1). The varied line shapes seen from transition to transition and molecule to molecule suggest a complicated relationship between the structure and the molecular emission. Several transitions have broad (>10 km s^{-1}) line widths indicating involvement in energetic activity, while others are narrow and may trace quiescent gas. Self-absorptions are also evident in several line profiles, appearing more frequently toward the S68 FIRS 1 source.

4. STRUCTURE AND CONDITIONS IN THE REGION

4.1. *The Northwestern Condensation*

A large-velocity gradient (LVG) radiative transfer code was used to model the single-dish data in order to provide density and column density estimates. The LVG model is a simplified treatment of the radiative transfer which is appropriate for deriving rough density and column density estimates when little is known about the cloud geometry (e.g., de Jong, Chu, & Dickinson 1975). The measured line temperatures for the CS

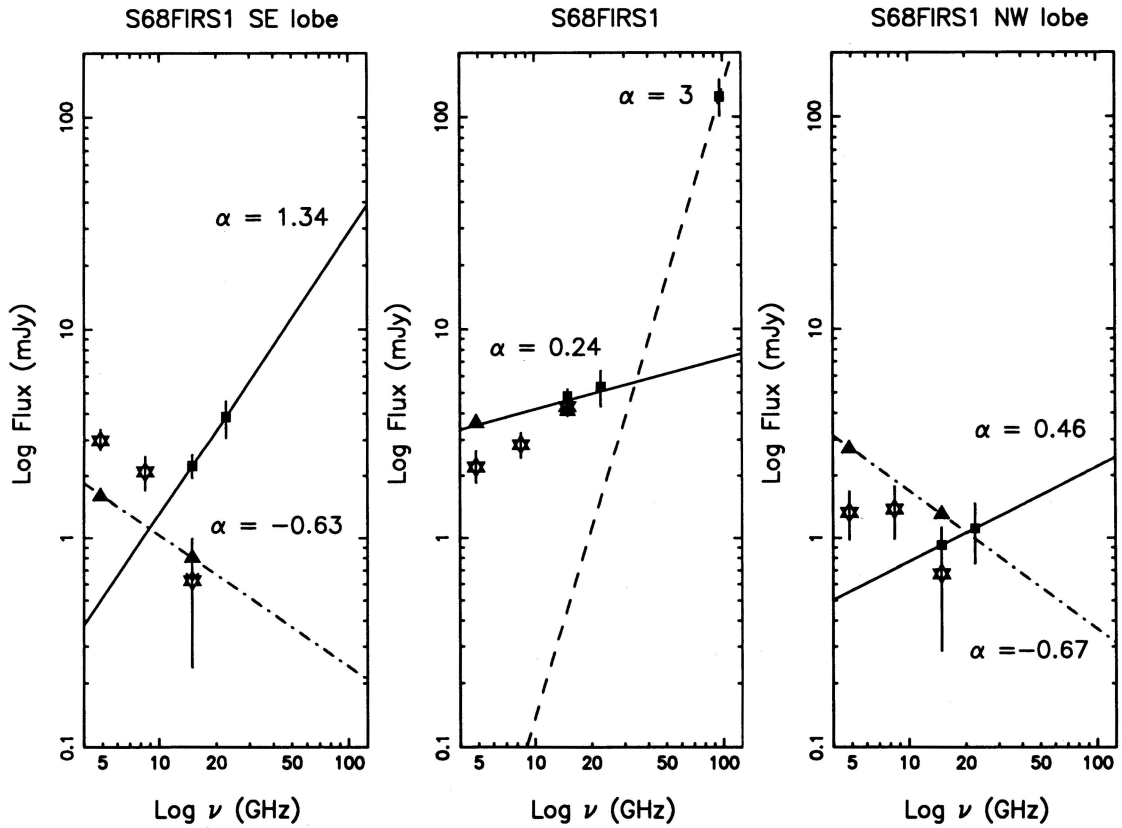

FIG. 8.—Centimeter continuum fluxes for each of three radio components of S68 FIRS 1. Solid squares indicate centimeter data from this study from the 1992 April observations; vertical lines extending from the squares mark the 2 σ error bars. Solid lines mark the least-squares fits to this study's data while the dot-dashed lines mark the fits to the data from Rodriguez et al. (1989). The open stars indicate data from this study taken in February of 1993. The differences between the open stars and the solid squares for the 15 GHz data indicate variability in the lobe emission on a timescale less than a year. For the center panel, the dashed line is $S_\nu \propto \nu^3$ power-law extrapolation to the millimeter data.

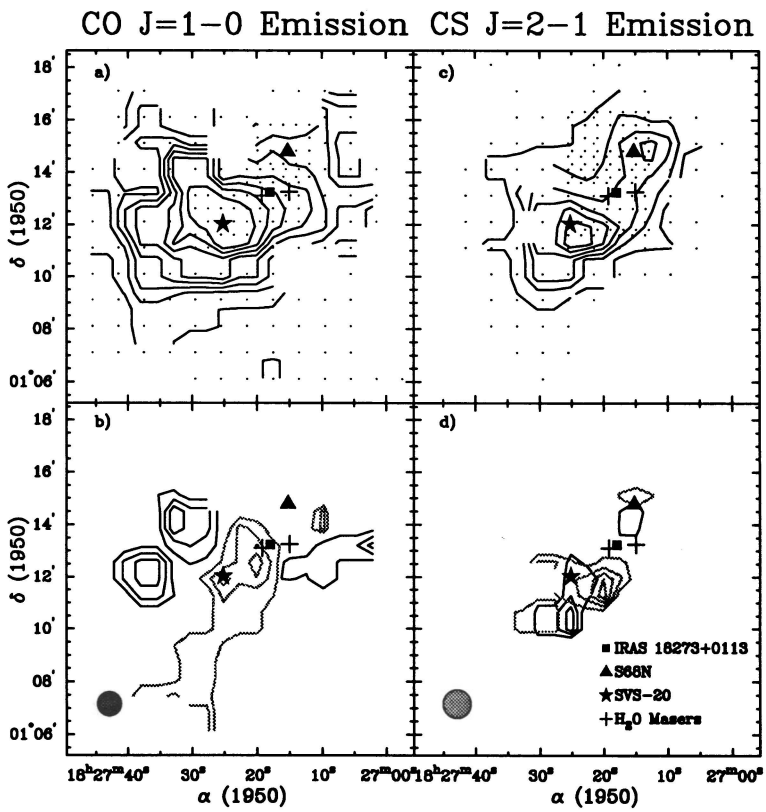

FIG. 9.—(*a*) CO $J = 1$–0 emission from the Serpens molecular core integrated from -4 to 20 km s^{-1}. Contour levels are in steps of 10 K km s^{-1}. (*b*) Wing emission in CO $J = 1$–0. Black contours mark redshifted emission integrated from 14 to 20 km s^{-1}; contours are in steps of 4 K km s^{-1}, starting at 4 K km s^{-1}. The gray contours mark blueshifted emission integrated from -4 to 2 km s^{-1} with contours in steps of 1 K km s^{-1}, starting at 4 K km s^{-1}. (*c*) Map of the integrated CS $J = 2$–1 emission. Contour levels are in steps of 2 K km s^{-1}. (*d*) Wing emission in CS $J = 2$–1. Black contours designate redshifted emission (integrated from 11 to 14 km s^{-1}) while the gray contours represent the blueshifted emission (integrated from 0 to 5 km s^{-1}). Contour levels are in steps of 0.2 K km s^{-1} for the red wing emission and in steps of 0.4 K km s^{-1} for the blue wing emission; contours start at 0.4 K km s^{-1}. The beam is represented in the lower left corner. Symbols are identical to those in Figs. 1 and 4.

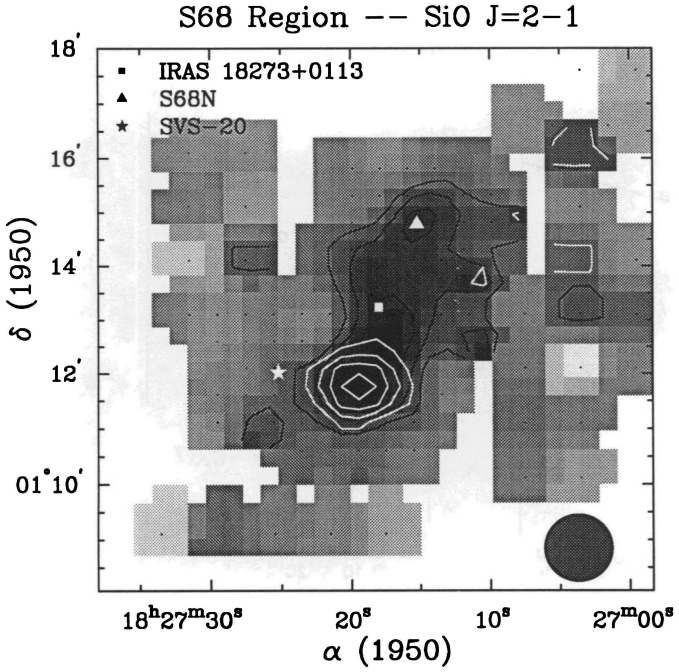

FIG. 10.—SiO $J = 2$–1 emission from the molecular core region. Grayscale and black contours mark emission integrated over the full line width of 11 km s^{-1}. Contours are in steps of 0.2 K km s^{-1}, starting at 0.4 K km s^{-1}. The overlaid white contours mark the blueshifted line emission, integrated from 0 to 5 km s^{-1}. Symbols are the same as in Fig. 9.

$J = 2 \rightarrow 1$, $J = 5 \rightarrow 4$, and $J = 7 \rightarrow 6$ transitions, $T_{MB} = 2.8$, 1.3, and 2.7 K, respectively, could not be fitted by a single density model. Instead, grids of column density and density were generated for the C^{34}S $J = 2 \rightarrow 1$ and $J = 5 \rightarrow 4$ lines using collision rates from Green (1991, private communication); the C^{34}S $J = 5 \rightarrow 4$ data were smoothed to the same resolution as the $J = 2 \rightarrow 1$ line. Adopting a temperature of 25 K from infrared observations (Zhang et al. 1988a) for the condensation, we derived a best-fit density of 3×10^5 cm^{-3} and a column density for C^{34}S of 3.6×10^{12} cm^{-2}. Assuming a terrestrial ratio of ^{32}S/^{34}S = 22.5, we obtain a CS column density of 8×10^{13} cm^{-2}. Temperature errors of ± 5 K cause $\sim 20\%$ errors in the density estimate.

Estimates for the mass and H_2 column density can be derived independently of the molecular line data based on the single-dish integrated millimeter continuum flux according to

$$N(\mathrm{H} + \mathrm{H}_2) = \frac{C_{250}}{\mu m_{\mathrm{H}}} \left(\frac{1.2 \times 10^{12}}{\nu} \right)^{\beta} \tau_{\nu} , \qquad (1)$$

and

$$M = 1.90 \times 10^{-3} C_{250} \left(\frac{1.2 \times 10^{12}}{\nu} \right)^{\beta+3} S_{\mathrm{Jy}} (e^{h\nu/kT_d} - 1) d_{\mathrm{kpc}}^2 \, M_{\odot} . \qquad (2)$$

In these equations, C_{250} represents the reciprocal of the mass opacity at $\lambda = 250$ μm in g cm^{-2}; we have adopted the value of

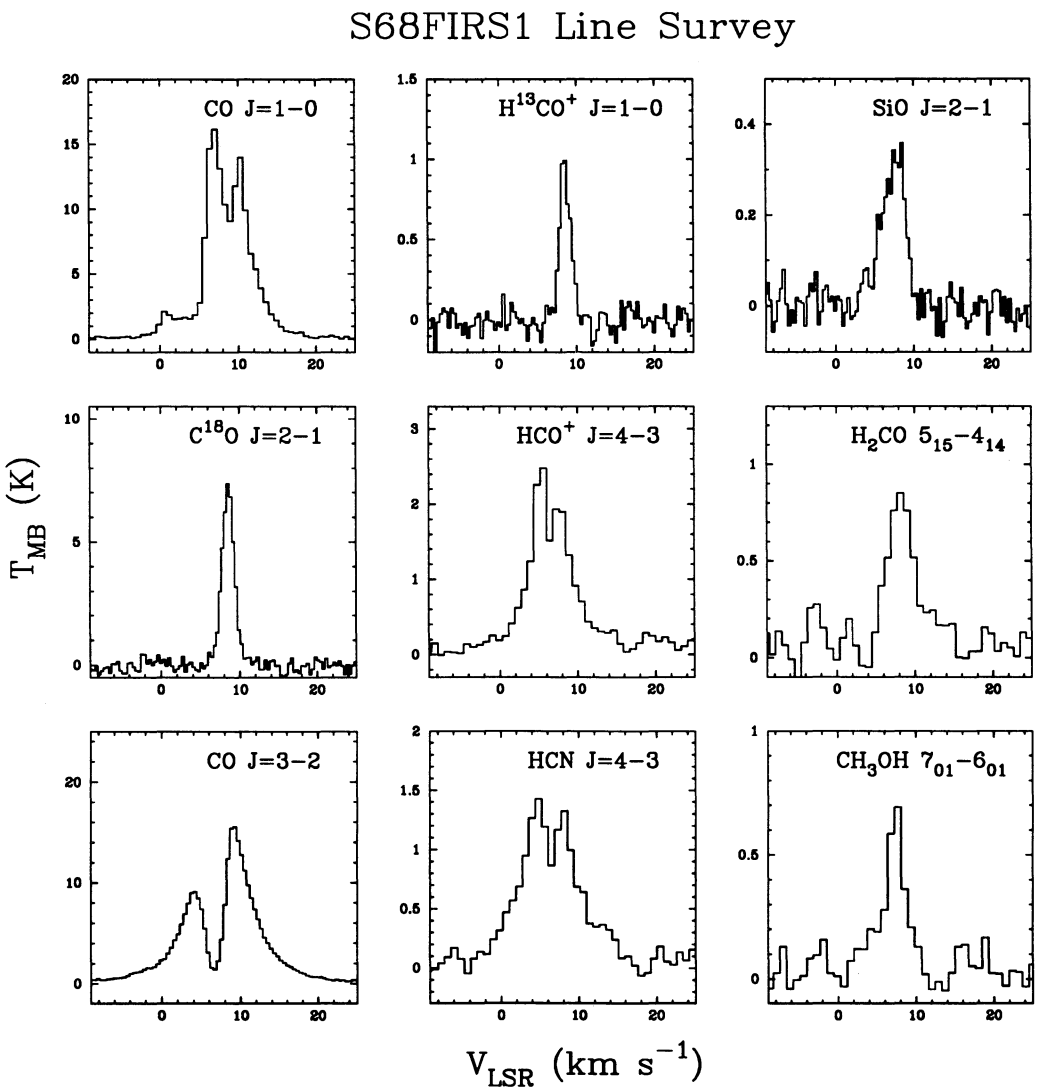

FIG. 11.—Molecular line survey toward S68 FIRS 1. Details of the observations are given in Table 1.

10 g cm^{-2} from Hildebrand (1983); β is the power-law index for the dust emissivity; m_H is the mass of a hydrogen atom; μ is the mean molecular weight, 2.72; τ_ν is the optical depth at the observing frequency; S_{Jy} is the integrated flux density in Jy; and d_{kpc} is the distance in kpc. Using $T_d = 25$ K, we derive a peak H_2 column density at $\lambda = 1.25$ mm for the condensation of 8.8×10^{22} cm^{-2} and a mass of 21 $M_\odot$, for $\beta = 2$ (Table 3). This value is likely to be a lower limit to the mass due to the limitations on the map area imposed by the 2′ chop. The derived mass and column density depend on the mass opacity coefficient, the wavelength dependence of the dust emissivity, and the dust temperature. For a detailed discussion of these effects, see Beckwith & Sargent (1991). The mass opacity and dust emissivity index represent the largest uncertainties, resulting in systematic uncertainties in our mass estimates of a factor of 2–4 (Drained 1990).

The mass of the condensation may be constrained in several other ways. Choosing a characteristic diameter of ~120″ (0.2 pc at 310 pc) based on the CS $J = 2 \rightarrow 1$ map, we derive a mass of ~62 $M_\odot$ assuming a spherical geometry and the density derived from the fitted C ^{34}S transitions. With this same diameter, we derive a virial mass ($R\Delta V^2/G$) of 68 $M_\odot$, using a characteristic line width of 1.8 km s^{-1}, as determined from C ^{34}S observations. Thus 70 $M_\odot$ is a reasonable estimate for the mass of this condensation. This value is higher than recent estimates for the total mass of the core (both NW and SE condensations) based on infrared (35 $M_\odot$, Zhang et al. 1988b) and NH_3 observations (60 $M_\odot$, Ungerechts & Güsten 1984) but significantly lower than an earlier estimate based on H_2CO observations (600 $M_\odot$, Loren et al. 1979).

Column densities of the molecular species in the chemical survey, N_x, were derived using the formula

$$N_x = \frac{3c^2}{16\pi^3\nu^3}\frac{Q(T)}{gu}\frac{\int S_\nu\, dv}{|\mu_{ul}|^2\Omega_B}\, e^{E_u/kT}, \qquad (3)$$

which assumes optically thin emission and local thermodynamic equilibrium. In this equation, $Q(T)$ is the partition function; g_u is the statistical weight of the upper level; Ω_B is the beam solid angle; E_u is the energy of the upper state; $|\mu_{ul}|$ is the dipole moment matrix element; $\int S_\nu\, dv$ is the peak integrated intensity in Jy beam^{-1} km s^{-1}, and T is the rotational excita-

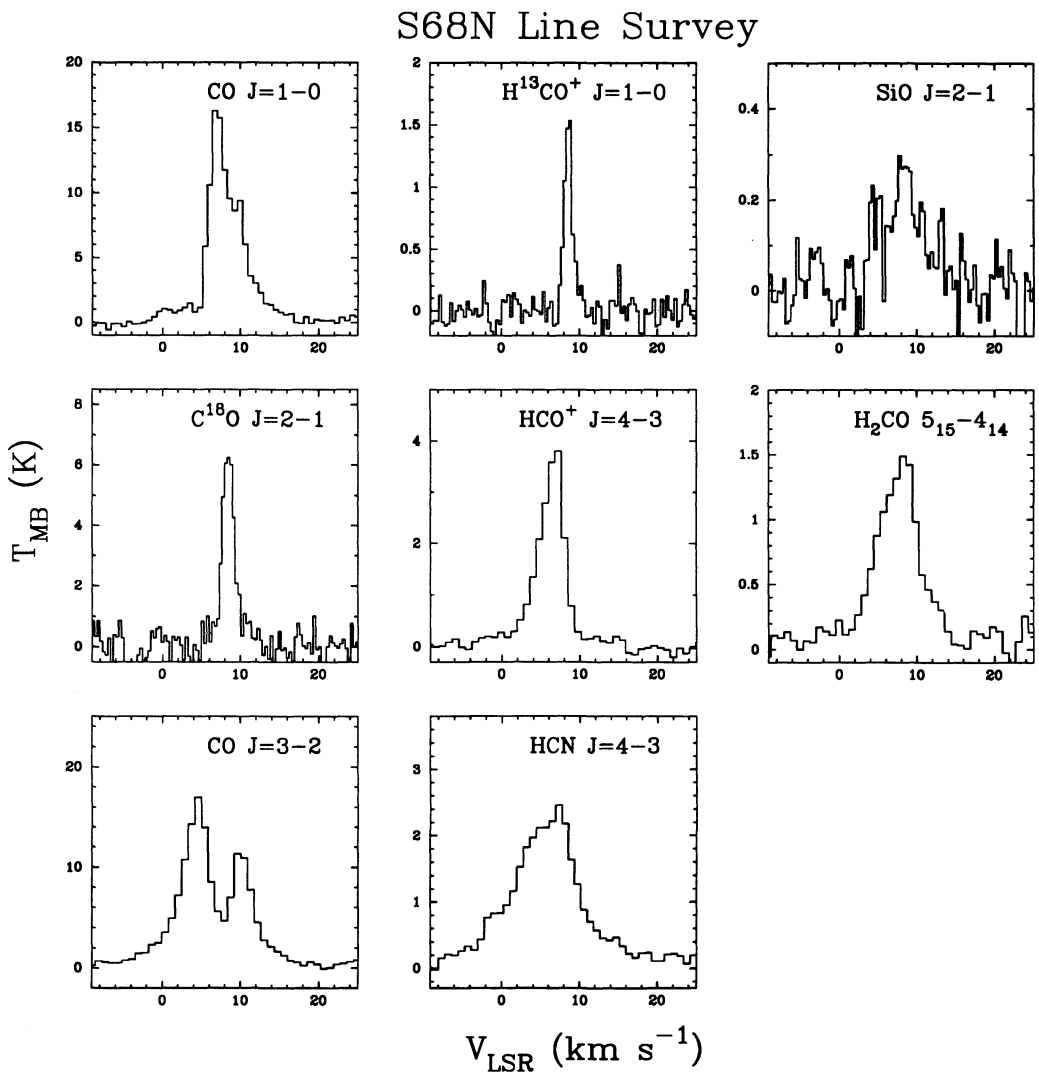

FIG. 12.—Molecular line survey toward S68 N. Details of the observations are given in Table 1.

TABLE 3

PROPERTIES OF THE NORTHWEST CONDENSATION

Quantity	Value
Assumed gas temperature[a]	25 K
Characteristic size	120″ (0.2 pc)
Characteristic density[b]	3×10^5 cm^{-3}
Peak continuum flux $\lambda = 1.25$ mm	2.3 Jy beam^{-1}
Integrated flux $\lambda = 1.25$ mm	6.5 Jy
Peak $N(H_2)$ from continuum flux[c]	1.2 (0.24) $\times 10^{23}$ cm^{-2}
Mass from continuum flux[c]	21 (4) $M_\odot$
Total virial mass	70 $M_\odot$
Peak CS column density[b]	8×10^{13} cm^{-2}
Peak HCM column density[d]	$>1.1 \times 10^{13}$ cm^{-2}
Peak CH_3OH column density[d]	4.4×10^{14} cm^{-2}
Peak H_2CO column density[d]	$\geq 1.9 \times 10^{13}$ cm^{-2}
Peak SiO column density[d]	3.9×10^{12} cm^{-2}
Peak CO column density[d,e]	3.6×10^{18} cm^{-2}
Peak HCO^+ column density[d,f]	3.6×10^{14} cm^{-2}

[a] Based on Loren et al. 1979 and Zhang et al. 1988a.
[b] Derived from LVG model; inferred from C ^{34}S.
[c] First value based on λ^{-2} emissivity; value in parenthesis is based on λ^{-1}. Both assume $C_{250} = 10$ g cm^{-2}.
[d] From eq. (1).
[e] Inferred from C ^{18}O; assumes $^{16}O/^{18}O = 489$.
[f] Inferred from H $^{13}CO^+$; assumes $^{12}C/^{13}C = 60$.

tion temperature. The partition function, energy of the upper state, dipole matrix element, and statistical weights were obtained from the line catalog of Poynter & Pickett (1984). Table 3 displays the derived peak column densities. We have attempted to utilize optically thin species whenever possible (C ^{18}O for CO, H $^{13}CO^+$, etc.); however, the self-absorbed line profile for HCN indicates that this species is probably optically thick and is therefore not sensitive to column density. The derived column density for H_2CO may also be optically thick based on its behavior in other regions of similar density.

4.2. *The Compact Sources*

In the following subsections, we focus on the small-scale structure of the northwestern condensation as revealed by the interferometer observations. Masses and H_2 column densities are derived from the $\lambda = 3.1$ mm continuum flux, based on equations (2) and (3). Column densities of the molecular gas species, N_x, are derived using equation (1). Since there is clearly a large amount of extended emission being resolved out, these column densities apply only to the material associated with the individual sources.

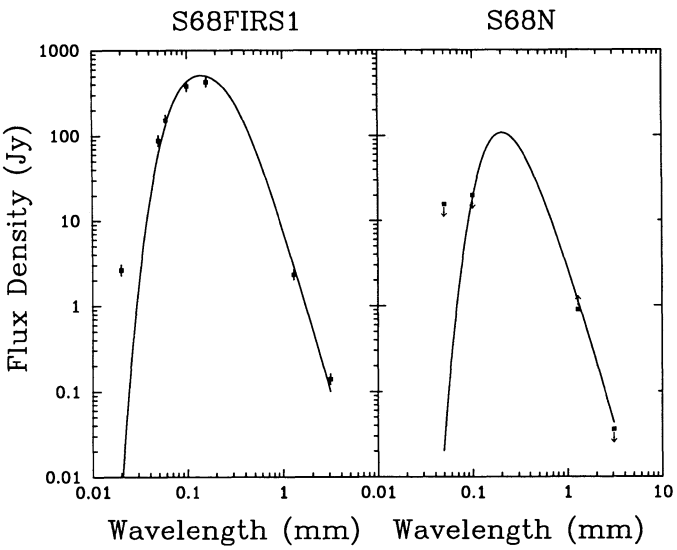

FIG. 13.—Spectral energy distributions for S68 FIRS 1 and S68 N. The left panel is a representative fit to S68 FIRS 1 using a dust temperature of 36 K, a λ^{-2} emissivity law, and a source size of 5″.6. The right panel is a representative fit to S68 N using a dust temperature of 16 K, a λ^{-2} emissivity law, and a 15″ source size. Data are listed in Table 2 with appropriate references.

4.2.1. *S68 FIRS 1*

Unique identification of S68 FIRS 1 in *IRAS* observations is difficult due to source confusion. Subsequent smaller beam, far-infrared studies by Harvey et al. (1984) and Zhang et al. (1988b) have shown that the far-infrared emission *does* peak at the FIRS 1 location; Harvey et al. (1984) assign a 100 μm flux of ~380 Jy to S68 FIRS 1, approximately half of the *IRAS* upper limit (Table 2). In the near-infrared, Eiroa & Casali (1989) failed to detect S68 FIRS 1 at either *H* or *L*′; however, an elongated, clumpy nebulosity, aligned with the larger scale molecular core, was detected nearby at *K*. The pointlike component of this emission, located well beyond the positional uncertainties of the radio continuum source, may represent another young star or scattered light from dust surrounding S68 FIRS 1 as has been suggested for other YSOs (Campbell et al. 1988; Ressler & Shure 1991).

To estimate a characteristic temperature for S68 FIRS 1, the spectral energy distribution was modeled as a uniform column density and temperature dust distribution; though this model is unphysical, it yields an approximate, mean temperature. Figure 13 displays a fit to the data for S68 FIRS 1; adequate fits were possible for temperatures in the range 32–40 K. Above and below these values, it was difficult to match the shape of the points from 50 to 160 μm; the 20 μm point could not be matched in any case, clearly indicating the presence of hotter dust. The temperatures derived are consistent with values in the literature (e.g., Zhang et al. 1988a). We obtain a luminosity for S68 FIRS 1 of 50–60 $L_\odot$, equivalent to a B9 ZAMS star (Thompson 1984) and a corresponding main-sequence stellar mass of ~3 $M_\odot$. An alternative lower limit to the central stellar mass may be obtained by assuming the central object is in pure accretion phase with an accretion rate of 10^{-5} $M_\odot$ yr^{-1} and a stellar radius of 3 $R_\odot$ (Stahler, Shu, & Taam 1980). Under these conditions, 50 $L_\odot$ can be produced by a 0.5 $M_\odot$ star. Our derived luminosity is significantly less than previous values in the literature (115 $L_\odot$, Harvey et al. 1984, scaled to our distance of 310 pc).

For the compact $\lambda = 3.1$ mm source, we can derive a column density and mass; values obtained using emissivity laws $\propto\lambda^{-2}$ or $\propto\lambda^{-1}$ (given in parentheses) are given in Table 4 along with the right ascension and declination of the position of peak continuum emission. This material lies within a region ~3800 AU in diameter which would include any circumstellar disk as well as inner regions of the circumstellar envelope. Adopting a temperature of 35 K, we derive an H_2 column density of 1×10^{24} cm^{-2} and a mass of 10.0 $M_\odot$ based on the Hildebrand relations with a λ^{-2} emissivity law. The mass derived represents less than 20% of the derived virial mass.

Based on these observations, the deduced masses of material and luminosity, S68 FIRS 1 appears to be a low-mass YSO. The high obscuration, relatively low temperatures, and lack of a strong signature on the molecular emission suggest a relatively early stage of evolution for the object.

4.2.2. *S68 N*

There is no clear *IRAS* counterpart for S68 N. IRAS 18272+0114 is located nearby, but has upper limits on all but the 12 μm flux due to source confusion. Harvey et al. (1984) shows that the 100 μm flux drops by a factor of ~10 toward S68 N. Zhang et al. (1988b) show that there is no distinct counterpart at *IRAS* wavelengths, though there is a definite extension of the maps from S68 FIRS 1 in that direction. Based on these observations and the positional offset between the *IRAS* source and the location of the molecular emission, we conclude that S68 N cannot be convincingly tied to any known *IRAS* point source. However, we can derive limits on the infrared emission based on the extensions seen in the 50 μm and 100 μm maps et al. (1988a), which may indicate the presence of a low-luminosity source at the position of S68 N (position obtained from the peak of the integrated CS map, Table 4). Using their contour maps to estimate an upper limit to the flux, along with our observations at $\lambda = 1.25$ and $\lambda = 3.1$ mm, we attempted to fit the continuum data as for S68 FIRS 1. Due

TABLE 4

PROPERTIES OF THE COMPACT SOURCES

Quantity	S68 FIRS 1	S68 N
Right ascension (1950)	$18^h27^m17^s.4$	$18^h27^m15^s.2$
Declination (1950)	01°13′16″.2	01°14′47″
Temperature	35 K	≤20 K
Peak $\lambda = 3.1$ mm continuum	140 mJy beam^{-1}	<36 mJy beam^{-1}
Peak $N(H_2)$ from continuum flux[a]	1.0 (0.08) × 10^{24} cm^{-2}	<0.4 (0.04) × 10^{24} cm^{-2}
Mass from continuum flux[a]	10.0 (0.8) $M_\odot$	<5 (0.4) $M_\odot$
CS column density	>0.6 × 10^{14} cm^{-2}	>1.1 × 10^{14} cm^{-2}
CH_3OH column density	<1.9 × 10^{15} cm^{-2}	1.5 × 10^{16} cm^{-2}

[a] First value based on λ^{-2} emissivity; value in parentheses is based on λ^{-1}. Both assume $C_{250} = 10$ g cm^{-2}.

to the combination of source size ($>10''$ according to interferometer observations) and low 100 μm flux, reasonable fits required a temperature of 20 K or less. The total luminosity is less than 5 $L_\odot$. We derive an upper limit to the mass of material based on the $\lambda = 3.1$ mm observations (Table 4). This limit is approximately a third of that seen for S68 FIRS 1.

It is difficult to be sure of the nature of S68 N from the available observations. The interferometric observations are sensitive to material on $\leq 60''$ scales, and the lack of continuum emission at $\lambda = 3.1$ mm implies the absence of a hot centrally condensed core. This, combined with the strong molecular gas emission, suggests that S68 N may be a molecular condensation which has not yet begun significant star formation.

4.3. *Material Traced by* SiO

The northwestern condensation is unusual in having much extended SiO emission. Chemical models predict that both high temperatures and shocks can produce enhancements in the gas-phase SiO abundance. Based on the abundance ratio of SiO to HCN in several molecular clouds Ziurys, Friberg, & Irvine (1989) deduced that SiO is formed by endothermic reactions with activation barriers around 90 K. Langer & Glassgold (1990) proposed a model which explains the sensitivity of SiO to high density and temperature as the dependence of the rate coefficients on the population of the excited fine-structure levels of the neutral Si atom. However, observations of low-temperature (~ 14 K) star-forming regions with SiO emission question this relationship (Bachiller, Menten, del Rio-Alvarez 1990; Bachiller, Martin-Pintado, & Fuente 1991). Martin-Pintado, Bachiller, Fuente (1992) suggest a shock-information mechanism in which grains are disrupted by a shock, thereby releasing Si into the gas phase allowing SiO to form via ion-molecule reactions or shock chemistry. Other models predict that fast molecular shocks will produce enhanced quantities of SiO in the cooling gas behind the dissociation region (Neufeld & Dalgarno 1989). Models of a fast neutral wind also produce significant amounts of SiO (Glassgold, Mamon, & Huggins 1989).

The SiO emission observed in the northwestern condensation shows a morphology which is more consistent with the shock scenario. The emission peak is offset from all of the known continuum sources in the region, but the overall emission is centered mostly about S68 FIRS 1 which is known to have an outflow (Rodriguez et al. 1989). If high temperatures alone were required for SiO formation, SiO emission should be strongest near SVS-20 and S68 FIRS 1. The peaking of both the integrated SiO emission and the blue-wing component to a region southeast of S68 FIRS 1 may indicate a region of strong interaction between the outflow and the surrounding material; the SiO blue wing is also traced by blue emission in CO and CS (Fig. 9). The orientation of the extended SiO emission, along the axis of the magnetic field (Gomez de Castro et al. 1988) and other outflow phenomena in the region (Eiroa & Casali 1989), is also suggestive of a shock origin. More observations at high spatial resolution are necessary to discern the exact role played by shocks.

5. CHEMISTRY

5.1. *Abundances*

Fractional abundances for the observed molecular species are given in Table 5. Values cited are based on the H_2 column density derived from the $\lambda = 1.25$ mm observations for the northwestern condensation and $\lambda = 3.1$ mm observations for the compact sources, using a λ^{-2} emissivity; values based on a λ^{-1} emissivity may be obtained by multiplying by a factor of 5 for the northwestern condenstation and a factor of ~ 12 for the compact sources. For the large beam observations taken at the NRAO 12 m (SiO, $H^{13}CO^+$, and CS) the $\lambda = 1.25$ mm continuum emission has been smoothed to a $\sim 60''$ beam yielding a peak continuum flux of 1.9 Jy beam^{-1} and a corresponding H_2 column density of 1.2×10^{23} cm^{-2} (2.4×10^{22} cm^{-2} for $\beta = 1$ law). For the CSO data (HCN, H_2CO, and CH_3OH) and for $C^{18}O$, the derived column densities were divided by the 30″ resolution H_2 column density given in Table 3. In the cases where the molecule may be optically thick, the values given denote *only* lower limits to the abundance. This includes HCN and H_2CO in the northwestern condensation, based on their profiles and observed opacities in other regions of similar density. For the compact sources, the CS emission may also be optically thick; hence the derived CS abundance represents a lower bound.

5.2. *Comparison with Other Regions*

Using the abundance for TMC-1 as a standard for quiescent gas, IRAS 16293−2422 as a standard for low-mass star-forming regions, and Orion-S and the Orion-KL hot core as high-mass star-forming standards with different amounts of chemical processing, we can examine the Serpens northwestern

TABLE 5

MOLECULAR FRACTIONAL ABUNDANCE[a]

MOLECULE	NW CONDITION	FRACTIONAL ABUNDANCE					
		S68 FIRS 1	S68 N	TMC-1[b]	IRAS 12693−2422[b]	Orion-S[c]	Orion-KL Hot Core[b]
CO	3.0 (−5)	...	...	8 (−5)	1 (−4)	...	1 (−4)
CS	6.7 (−10)	>6 (−11)	>3 (−10)	1 (−8)	1 (−9)	>3 (−10)	>1 (−8)
SiO	3.3 (−11)	...	...	<2 (−12)	1 (−10)	<5 (−12)	
HCO^+	3.0 (−9)	...	...	6 (−9)	1 (−9)	9 (−10)	<1 (−9)
CH_3OH	3.7 (−9)	2 (−9)	<4 (−8)	2 (−9)	2 (−9)	1 (−9)	(0.1–1) (−6)
HCN	>9.2 (−11)	...	...	1 (−8)	7 (−10)	...	2 (−7)
H_2CO	1.6 (−10)	...	...	2 (−8)	1 (−9)	...	>6 (−8)

[a] Abundances listed are derived from N_{H_2} based on a λ^{-2} emissivity. Multiply by a factor of 5 to obtain abundances based on a λ^{-1} emissivity.

[b] Taken from Van Dishoeck et al. 1992 & Blake et al. 1993.

[c] Taken from McMullin et al. 1993.

condensation within this chemical context. For two of the three molecular abundances derived from optically thin isotopic species, CO and HCO^+, the derived abundances are consistent with those measured in both quiescent and star-forming regions. The third molecule, CS, indicates gas-phase depletions of factors of ~ 10 when compared to the quiescent region and the Orion-KL hot core but not compared to other star-forming regions (IRAS 16293−2422 and Orion-S). HCN and H_2CO, though lacking necessary isotopic information, would require large opacities (>10) to avoid being depleted. The measured CH_3OH abundance is within a factor of 2 of quiescent and low-mass star-forming regions but 2–3 orders of magnitude lower than the more processed Orion-KL hot core. The SiO abundance is intermediate between that found in other star-forming regions and similar to TMC-1. Interestingly however, the SiO emission has substantially different *morphologies* in each of these sources, and in general does not follow the H_2 column density. If SiO is distributed only in shocks, then only a small fraction of the column within the beam is emitting, leading to much higher abundances than listed within the SiO emitting gas. Using the CO and SiO emission from 0 to 5 km s^{-1} to trace the shocked gas, we derive a column density ratio, $N(SiO)/N(CO)$ of 2×10^{-4}, a relative abundance similar to the Orion-KL outflow (plateau region). Though this value is somewhat uncertain due to optical depth in the CO line, it suggests that the high-velocity gas may be chemically differentiated from the surrounding material.

A similar comparison may be performed using relative abundance ratios with respect to CO (N_x/N_{CO}), independent of the H_2 column density as derived from continuum observations. These results are similar with those from the absolute fractional abundances; that is, H_2CO and HCN seem to be depleted while the CS abundance appears similar to that in the IRAS 16293−2422 and Orion-S regions. The CH_3OH shows intermediate values between the quiescent and star-forming regions. In contrast to the previous absolute abundance comparison, HCO^+ shows a distinct enhancement with respect to the star-forming regions but not compared to the quiescent regions.

It is now clear that both infall and outflow motions are characteristic of star formation (Shu et al. 1993), raising the possibility that both accretionary and shock processes modify the chemical composition of YSOs. Although outflow activity is readily identified in star-forming environments (e.g., Lada 1985), infall activity and the corresponding chemical changes wrought from infall such as gas-phase depletions (e.g., Rawlings et al. 1992) have been far more difficult to prove. Despite this, depletions have been noted in a number of star-forming regions (e.g., Mauersberger et al. 1992; Blake, van Dishoeck, & Sargent 1992; Goldsmith et al. 1992). During the early stellar stages, depletion of gas-phase tracer molecules onto grain mantles can occur rapidly at high densities. As the YSO begins to heat up its surroundings, and as energetic phenomena are initiated, material from the grain surfaces returns to the gas phase, returning abundances to "normal." High-temperature chemical pathways and further grain disruption can lead to enhancements in specific molecules, relative to a quiescent cloud. Our data do not indicate strong gas-phase depletions in the overall northwest condensation. The most convincing cases for depletion are HCN and H_2CO where the observed transitions are likely to be optically thick. Future observations of isotopic species, and especially high-resolution observations of isotopic species, will help to resolve this issue. If no depletions are supported, it raises the question of over what scales depletions may be found, that is, does depletion occur on the larger scale of the extended condensation or only toward the most compact, star-forming sources?

The derived abundances in compact sources are complicated by potentially high opacities in CS and nondetections of CH_3OH toward S68 FIRS 1 and of $\lambda = 3.1$ mm continuum emission toward S68 N. It is interesting to note, however, that the lower limit on the methanol abundance toward S68 N is mildly enhanced relative to most of the regions listed. If this is a true abundance enhancement, it is inconsistent with its otherwise cold, quiescent nature. Methanol is thought to arise from regions of mild outflow interaction, where grain mantles are gently evaporated, leading to enhanced gas-phase abundances (e.g., Millar, Herbst, & Charnley 1991). Recent observations also indicate large enhancements in the abundance of methanol at the location of the outflow tip, as seen in NGC 1333 IRAS 2 (Sandell 1993). Interpreting the abundance in the methanol transition is complicated by the fact that this transition has been identified as a masing line (class I; Menten 1991). However, our observations show no evidence of this in S68 N. Class I masers are characteristically offset from other continuum and molecular line peaks (e.g., Plambeck & Menten 1990; Batrla & Menten 1988; Menten et al. 1986), but in S68 N, the methanol and CS peaks are coincident. Observations of this masing transition in Orion-KL and DR 21 [and DR 21 (OH)] show narrow lines (<1 km s^{-1}) with brightness temperatures of several hundred degrees. The methanol spectrum of S68 N, with a velocity resolution of 0.25 km s^{-1}, shows no narrow spikes superposed on the 3 km s^{-1} wide line. We conclude that the observed methanol emission is thermally excited. Since the observed transition sits over 80 K above the ground state and is high above the base of the K ladder, it is difficult to obtain excitation effects which could mimic an enhanced abundance. Though our lack of a well-constrained value for the H_2 column density precludes further analysis, this source remains a puzzle for later observations to solve.

6. SUMMARY

We have used single-dish and interferometric observations of the northwestern condensation in the Serpends molecular cloud core to derive characteristic properties for the condensation and the two compact emission regions, and to understand the interaction between the large- and small-scale components of this star-forming region. Based on the large- and small-scale distributions of CS and dust continuum emission, only a small fraction of the condensation is directly associated with S68 FIRS 1 and S68 N. The preponderance of mass in an extended, high-density component suggests that the overall condensation is still at an early evolutionary state. Derived abundances for CO and HCO^+ in the northwestern condensation are consistent with quiescent and other star-forming regions. The CS, HCN, and H_2CO observations indicate mild gas-phase depletions though our data are insufficient to clearly establish their existence.

The observed SiO $J = 2 \rightarrow 1$ emission is localized to a southeast-northwest ridge, aligned with the magnetic field (Gomez de Castro et al. 1989) and other outflow phenomena (radio continuum lobes, H_2 emission, near-infrared nebulosities around other pre–main-sequence objects) and the likely outflow axis of S68 FIRS 1. We interpret this morphology and the offset of the peak emission from any of the known infrared

sources as consistent with a shock rather than a high-temperature origin for the formation of this molecule.

S68 FIRS 1, a deeply embedded YSO, is characterized by a temperature of $\sim$35 K and a modest luminosity of $\sim$50–60 $L_\odot$. The derived H_2 column density is consistent with expectations for a deeply embedded infrared source. The circumstellar gas and dust mass implied by the $\lambda = 3.1$ mm observations is $\sim 10\ M_\odot$ within a region less than 3800 AU. These derived properties for S68 FIRS 1 are consistent with a 0.5–3.0 $M_\odot$ mass YSO, still surrounded by most of its embryonic material.

Radio continuum observations of the triple source toward S68 FIRS 1 indicate that the emission from the lobes is variable. Observations separated by less than a year indicate drastic changes in both the strength and spectrum of the emission in the lobes; in contrast, the central component's emission is found to be roughly constant at $\lambda = 2.0$ cm over a period of approximately 14 years. It is important to monitor the variability in this source and begin to rigorously probe the physics of the radio lobes.

For S68 N, the loosely constrained spectral energy distribution indicates a dust temperature of $\leq$20 K and a total luminosity of $\leq 5\ L_\odot$. The apparent lack of significant internal heating, along with the strong molecular emission, suggests that S68 N may have little or no current star formation; however, the lower bound to the CH_3OH abundance in this region is similar to the chemically active, Orion compact ridge, possibly indicating interaction with external outflows. If this object truly represents a prestellar condensation as its weak dust emission suggests, S68 N may provide new insights into the chemical and density evolution directly preceding the formation of a protostar.

We would like to thank the following individuals whose help was important in obtaining the large amount of observations necessary for this project: Phil Jewell and the telescope operators of the NRAO 12 m; Tom Phillips, Jocelyn Keene, and Antony Schinkel (CSO); Rick Forster, Marc Warnock, and Al Masters (BIMA); Barry Clark (VLA). Special thanks to T. Groesbeck, J. Howe, and T. Helfer for help with observations. This work was sponsored by National Science Foundation grant AST 91-00306 and by NASA grant 01526111. G. A. Blake acknowledges support from the David & Lucille Packard and Alfred P. Sloan Foundations, and NASA grant NAGW-2297

REFERENCES

Allen, L. E., Snell, R. L., Schloerb, F. P., & Heyer, M. H. 1989, BAAS, 20, 1060
Andre, Ph., Montmerle, T., Feigelson, E. D., & Steppe, H. 1990, A&A, 240, 321
Bachiller, R., Martin-Pintado, J., & Fuente, A. 1991, A&A, 243, L21
Bachiller, R., Menten, K., & del Rio-Alvarez, S. 1990, A&A, 236, 461
Bally, J., & Lada, C. J. 1983, ApJ, 265, 824
Batrla, W., & Menten, K. M. 1988, ApJ, 329, L117
Blake, G. A., Sutton, E. C., Masson, C. R., & Phillips, T. G. 1987, ApJ, 315, 621
Blake, G. A., van Diskhoeck, E. F., Jansen, D. J., Groesbeck, T., & Mundy, L. G. 1993, ApJ in preparation
Blake, G. A., van Dishoeck, E. F., & Sargent, A. I. 1992, ApJ, 391, L99
Beckwith, S. V. W., & Sargent, A. I. 1991, AJ, 381, 250
Campbell, B., Persson, S. E., Strom, S. E., & Grasdalen, G. L. 1988, AJ, 95, 1173
Churchwell, E., & Koorneef, J. 1986, ApJ, 300, 729
Crusius-Watzel, A. 1990, ApJ, 361, L49
Curiel, S., Rodriguez, L. F., Moran, J. M., & Canto, J. 1993, ApJ accepted
de Jong, T., Chu, S., & Dalgarno, A. 1975, ApJ, 199, 69
de Lara, E., Chavarria-K, C., & Lopez-Molina, G. 1991, A&A, 243, 139
Dinger, A. S., & Dickinson, D. F. 1980, AJ, 85, 1247
Draine, B. T. 1990, in The Interstellar Medium in Galaxies, ed. H. A. Thronson & J. M. Shull (Dordrecht: Kluwer), 483
Eiroa, C., & Casali, M. M. 1989, A&A, 223, L17
———. 1992, A&A, 262, 468
Eiroa, C., Lenzen, R., Leinert, Ch., & Hodapp, K.-W. 1987, A&A, 179, 171
Fuller, G. A., & Ladd, E. F. 1992, BAAS, 24, 1200
Glassgold, A. E., Mamon, G. A., & Huggins, P. J. 1988, ApJ, 336, L29
Goldsmith, P. F., Margulis, M., Snell, R. L., & Fukui, Y. 1992, ApJ, 385, 522
Gomez de Castro, A. I., Eiroa, C., & Lenzen, R. 1988, A&A, 201, 299
Green, S. 1988, private communication
Harvey, P. M., Wilking, B. A., & Joy, M. 1984, ApJ, 278, 156
Henriksen, R. N., Ptushkin, V. S., & Mirabel, I. F. 1991, A&A, 248, 221
Hildebrand, R. H. 1983, QJRAS, 24, 267
Ho, P. T. P., & Barrett, A. H. 1980, ApJ, 237, 38
Jewell, P. R. 1988, NRAO 12 meter Telescope Receiver and Calibration Status
Keene, J. 1991, private communication
Kutner, M. L., & Ulich, B. L. 1981, ApJ, 250, 341
Lada, C. 1985, ARA&A, 23, 267
Langer, W. D., & Glassgold, A. E. 1990, ApJ, 352, 121
Little, L. J., Brown, A. T., McDonalds, G. H., Riley, P. W., & Matheson, D. N. 1980, MNRAS, 193, 115
Loren, R. B., Evans, N. J., II, & Knapp, G. R. 1979, ApJ, 234, 932
Martin-Pintado, J., Bachiller, R., & Fuente, A. 1992, A&A, 254, 315
Martin-Pintado, J., Rodriguez-Franco, A., & Bachiller, R. 1990, ApJ, 357, L49
Mauersberger, R., Wilson, T. L., Mezger, P. G., Gaume, R., & Johnston, K. J. 1992, A&A, 256, 640
McMullin, J. P., Mundy, L. G., & Blake, G. A. 1993, ApJ, 405, 599
Menten, K. M. 1991, in Skylines, Proc. Third Haystack Observatory Meeting, vol. 16, ed. A. D. Haschick, P. T. P. Ho (San Francisco: Astronomical Society of the Pacific), 119
Menten, K. M., & Batrla, W. 1989, ApJ, 341, 839
Millar, T. J., Herbst, E., & Charnley, S. B. 1991, ApJ, 369, 147
Mirabel, I. F., Ruiz, A., Rodriguez, L. F., & Canto, J. 1987, ApJ, 318, 729
Neufeld, D. A., & Dalgarno, A. 1989, ApJ, 340, 869
Nordh, H. L., van Duinen, R. J., Sargent, A. I., Fridlund, C. V. M., Aalders, J. W. G., & Beintema, D. 1982, A&A, 115, 308
Plambeck, R. L., & Menten, K. M. 1990, ApJ, 364, 555
Plambeck, R. L., & Wright, M. C. H. 1987, in Molecular Clouds in the Milky Way and External Galaxies, ed. R. L. Dickman, R. L. Snell, & J. S. Young (New York: Springer), 182
Poynter, R. L., & Pickett, H. M. 1984, Submillimeter, Millimeter, and Microwave Spectral Line Catalogue, JPL Pub. 80-23, Rev. 2
Rawlings, J. M. C., Hartquist, T. W., Menten, K. M., & Williams, D. A. 1992, MNRAS, 255, 471
Ressler, M. E., & Shure, M. 1991, AJ, 102, 1398
Rodriguez, L. F., Curiel, S., Moran, J. M., Mirabel, I. F., Roth, M., & Garay, G. 1989, ApJ 346, L85
Rodriguez, L. F., Moran, J. M., Ho, P. T. P., & Gottlieb, E. W. 1980, ApJ, 845
Sandell, G. 1993, private communication
Shu, F., Najita, J., Galli, D., & Ostriker, E. 1992, in Protostars and Planets III, ed. E. H. Levy & J. I. Lunine (Tucson: Univ. Arizona Press), 3
Snell, R. L., & Bally, J. 1986, ApJ, 303, 683
Stahler, S. W., Shu, F. H., & Taam, R. E. 1980, ApJ, 242, 226
Strom, S. E., Grasdalen, G. L., & Strom, K. M. 1974, ApJ, 191, 111
Strom, S. E., Vrba, F. J., & Strom, K. M. 1976, AJ, 81, 638
Thompson, R. I. 1984, ApJ, 283, 165
Torrelles, J. M., Gómez, J. F., Curiel, S., Eiroa, C., Rodríguez, L. F., & Ho, P. T. P. 1992, ApJ, 384, L59
Elich, B. L. 1981, AJ, 86, 1619
Ulich, B. L., Dickel, J. R., & de Pater, I. 1984, Icarus, 60, 590
Ungerechts, H., & Gušten, R. 1984, A&A, 131, 177
Van Dishoeck, E. F., Blake, G. A., Draine, B. T., & Lunine, J. I. 1992, in Protostars and Planets III, ed. E. H. Levy, J. I. Lunine, & M. S. Matthews (Tucson: Univ. Arizona Press), 163
Walker, C. K., Adams, F. C., & Lada, C. J. 1990, ApJ, 349, 515
Wilking, B. A., Lada, C. J., & Young, E. T. 1989, ApJ, 340, 823
Zhang, C. Y., Laureijs, R. J., & Clark, F. O. 1988a, A&A, 196, 236
Zhang, C. Y., Laureijs, R. J., Clark, F. O., & Wesselius, P. R. 1988b, A&A, 199, 170
Ziurys, L. M., Friberg, P., & Irvine, W. M. 1989, ApJ, 343, 201